Changes in the Global Climate: Atmospheric Angular Momentum and Pacific Ocean Temperatures

KLAUS WEICKMANN,[a] EDWARD BERRY,[b] VICTOR GENSINI,[c] DAVID GOLD,[d] AND THOMAS PETROSKI[e]

[a] *Boulder, Colorado*
[b] *Marion, Iowa*
[c] *Northern Illinois University, DeKalb, Illinois*
[d] *IBM Consulting, Houston, Texas*
[e] *DTN LLC, Norman, Oklahoma*

(Manuscript received 10 May 2022, in final form 13 June 2023, accepted 13 June 2023)

ABSTRACT: Atmospheric angular momentum (AAM) is used to study the variability of Earth's atmospheric circulation during the past 45 years, a time of considerable climate change. Using global AAM, two interdecadal states are defined covering the periods 1977–98 (hereinafter P1) and 1999–2022 (P2). Global AAM decreased from P1 to P2 and was accompanied by weakened subtropical jet streams in both hemispheres, strong convection around the northern Maritime Continent, and a strengthened sea surface temperature (SST) gradient across the tropical Pacific Ocean. The period differences project onto 1) internal interdecadal Pacific variability (IPV), 2) a postulated transient ocean thermostat response to greenhouse gas and aerosol emissions, and 3) circulation anomalies related to the ozone hole. During 1977–2023, the first two processes are forcing the climate toward larger Pacific Ocean SST gradients and a poleward expansion of the Indo-Pacific warm pool (IPWP), especially into the Northern Hemisphere. The ozone hole produces its own distinct pattern of anomalies in the Southern Hemisphere that tend to become persistent in the early 1990s. The zonal and vertical mean AAM variations during P1 have frequent westerly wind anomalies between 40°N and 40°S with poleward propagation on interannual time scales. During P2, the circulation is dominated by subtropical easterly wind anomalies, poleward-shifted jets, and weaker propagation. Locally, the zonal mean anomalies manifest as midlatitude ridges that lead to continental droughts. Case studies illustrate the weakened subtropical jet streams of P2 and examine the factors behind a transition to La Niña in early 2020 that maintains the P2 pattern.

KEYWORDS: Atmospheric circulation; Angular momentum; Climate change; Climate variability

1. Introduction

Atmospheric angular momentum (AAM) has been used to study changes in the global circulation on multiple time scales ranging from synoptic to millennial (Paek and Huang 2012; Veerman and Heerwaarden 2019). AAM is a measure of the rotation of the atmosphere about Earth's axis and is altered through exchanges with the solid Earth also rotating about its axis (Peixoto and Oort 1992). Changes in this quantity are related to surface wind stresses, surface pressures across complex terrain (Weickmann 2003; Weickmann and Sardeshmukh 1994, hereinafter WS94; Weickmann et al. 1997; Egger et al. 2007) and indirectly meridional AAM transports (Palmen and Newton 1969; Starr 1948, 1951).

Numerous studies of global and zonal mean AAM have been carried out using various model and reanalysis datasets. These include relationships between global AAM and the length of day (Rosen and Salstein 1983; Salstein et al. 1993), changes in AAM as a function of the El Niño–Southern Oscillation (ENSO; Rosen et al. 1984; Dickey et al. 1992), and variations of zonal and global AAM due to 30–70-day activity (Weickmann et al. 1997). Global mean relative AAM is anomalously high during an El Niño and certain phases of the Madden–Julian oscillation (MJO; Madden and Julian 1971, 1972, 1994) due to anomalous zonal mean westerly wind flows in the subtropical atmosphere; the opposite flows and low AAM occur during La Niña and certain phases of the MJO.

In this investigation, climate changes related to two Pacific Ocean climate shifts in 1976/77 and 1998/99 are studied, where Period 1 (P1) is defined as 1977–98 and Period 2 (P2) is defined as 1999–2022. The shifts have been associated with opposite phases of the interdecadal Pacific oscillation (IPO; Meehl et al. 2016a; Folland et al. 2002) and possibly also with a transient response to greenhouse gas and aerosol emissions (Heede and Fedorov 2023) related to the ocean thermostat hypothesis. This would help explain the difference between the current climate, represented here by P2, and the climate predicted by climate models, which is closer to P1 (Heede et al. 2021).

Interdecadal and decadal variations of the atmosphere and ocean have been studied extensively dating back to at least the late 1800s (e.g., Nigam et al. 2020; Dong and Dai 2015; Paek and Huang 2012; Veerman and Heerwaarden 2019;

Denotes content that is immediately available upon publication as open access.

Weickmann: Retired.

Berry: Deceased.

Corresponding author: Klaus Weickmann, klaus.weickmann@gmail.com

DOI: 10.1175/JCLI-D-22-0322.1

Yang et al. 2020; Moron et al. 1998; Meehl et al. 2016a). For the IPO, Henley et al. (2015) suggest warm or positive phases were observed during roughly 1924–44 and 1977–99, and negative or cold phases during 1945–76 and 1999–2013. The negative or cold phases had anomalously high sea level pressure across the central and eastern North Pacific Ocean with the opposite sense during the positive or warm phase. Broadly speaking, the negative phase has the characteristics of La Niña while the positive phase resembles El Niño. This has led to the idea of La Niña–like and El Niño–like states lasting for decades.

The IPO is also known as interdecadal Pacific variability (IPV) since the mode may not be an oscillation; it could be a red noise process with a 3–5-yr decay time scale. Tung et al. (2019) even dispute the existence of an interdecadal Pacific SST mode, preferring the well-known Pacific decadal oscillation (PDO/PDV) based on temporal filtering and rotated EOFs. Meehl et al. (2021) studied large member composites of model IPO transitions but did not characterize the type of temporal variability. We will use the above acronyms interchangeably, somewhat dependent on their use in the reference being cited.

After the first climate shift in 1976/77, the Indo-Pacific warm pool (IPWP) expanded eastward (Roxy et al. 2019; Hartmann and Wendler 2005) creating a favorable ocean state for basin-wide El Niño (warm) events involving the eastern Pacific cold tongue including the strong 1982/83 and 1997/98 events. Related to this warm pool expansion the positive phase of the IPO/IPV/PDO dominated much of 1977–98 (Meehl et al. 2016a; Henley et al. 2015).

After the second climate shift in 1998/99, the IPWP center moved northwest and expanded poleward as the negative phase of IPV/IPO prevailed (Dong and Dai 2015). There is the suggestion that "global warming" pauses when IPV is in its negative phase (i.e., P2) leading to a "warming hiatus" (Medhaug et al. 2017) such as was observed during 2000–15. After the 2015/16 El Niño, Su et al. (2017) and Hu and Fedorov (2017) proposed global surface temperature had exited the hiatus with a transition to positive IPO. Several models (Henley et al. 2017; Meehl et al. 2016b; Thoma et al. 2015) also predicted that the IPO would return to a positive phase during 2015–19 and resume an accelerated warming. The 3-yr La Niña that developed in early 2020 leaves that result in doubt. Although variability has increased, little additional warming in global temperatures has occurred since the 2015/16 El Niño.

Fasullo et al. (2023) postulate transient forcing from the 2019/20 Australian wildfire smoke helped force the La Niña and shifted the climate back to a negative IPO. A diagnosis of AAM and outgoing longwave radiation (OLR) anomalies during the onset of the 2019/20 La Niña (section 7) suggests that typical ENSO variability was at play. Less typical were the effects from the ozone hole in Southern Hemisphere circulation, especially since ~1993 when it reached its maximum areal extent and remains nearly that large through 2022. The downward coupling from the strong jet in the stratosphere that accompanies the decreased heating in the southern polar stratosphere reaches the surface in December–February (Orr et al. 2021) and interacts with the internal (IPO/IPV) and forced (greenhouse gases and aerosols) variability discussed earlier.

The paper is organized as follows. Section 2 presents a short review of the AAM calculations and summarizes the datasets and analysis techniques. The two interdecadal periods, P1 and P2, are described in section 3 using AAM and Pacific Ocean SST anomalies. Section 4 presents period mean anomaly maps while section 5 compares the differences in climatology for AAM and 500-hPa heights. In section 6 a case study illustrates the P2 preferred anomaly pattern during 2019–21 and the impact from a weak El Niño in 2019/20 and a moderate La Niña in 2020/21. Section 7 summarizes and discusses the main points.

2. Data and analyses

a. *Zonal and global AAM integrals*

The complete equations for the zonal and global AAM budget are presented in WS94. The zonal and global integrals of daily relative AAM from 1958 to 2022 are used to define two interdecadal states and to study climate features of two recent winters. The global relative AAM is defined by

$$M_r = \langle [\{u \times a \times \cos(\phi)\}] \rangle, \tag{1}$$

whereas the zonal relative AAM is

$$m_r(\phi) = [\{u \times a \times \cos(\phi)\}], \tag{2}$$

where {}, [], and $\langle\rangle$represent vertical, zonal, and meridional integrals, respectively (see WS94); u is the zonal wind, a is the radius of Earth, and ϕ is latitude.

Accordingly, vertical integrals are computed for each latitude–longitude grid box, and these are summed appropriately to make any area or volume integral. Thus, the units on AAM are the same whether zonal or global integrals ($\mathrm{kg\,m^2\,s^{-1}}$); this is true likewise for the AAM tendency where the units are $\mathrm{kg\,m^2\,s^{-2}}$.

The AAM climatology is defined for the period 1977–2022 and is used to compute the anomalies shown in Figs. 1 and 7 (below). The 1977–2022 climatology allows anomalies to be compared directly between the two periods. If climatology were defined as P1 or P2, anomalies in the opposite period would become inflated. For example, the climatology currently being used by diagnostic and forecast centers covers 1991–2020. As a result, the significant warming from this period is now part of the climatology and is no longer seen in the anomalies with the last 30-yr climatology removed. The years before 1991 now have inflated negative anomalies relative to the warmer 1991–2020 climatology.

For the P2 − P1 change in climatology (Figs. 5 and 6, discussed in more detail below), we compute the difference between the climatology (all harmonics) of each period. Only the 1968–2022 portion of the NCEP–NCAR reanalysis (R1) AAM is used due to an assimilation problem with 1948–67 that produces a spurious negative mountain torque in the NH as discussed in the appendix. On the other hand, the positive mountain torque seen along 10°–30°S in Fig. A1a is real and develops around the time that the ozone hole reaches its maximum areal extent

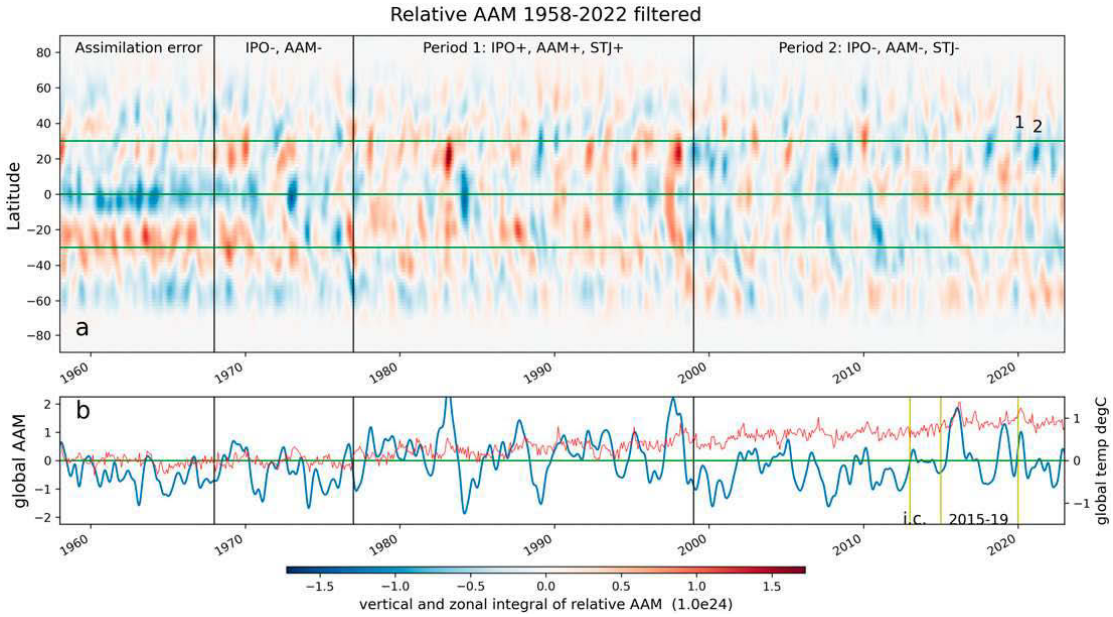

FIG. 1. The (a) zonal and (b) global relative AAM anomalies for January 1958–2022. The daily zonal and global fields have been filtered with a 300-day low-pass Gaussian filter. The vertical lines separate periods that are characterized by the text on the top of (a) ("period 1" is defined as 1977–98, and "period 2" is defined as 1999–2022). For reference, two recent easterly wind episodes (15°–35°N) are numbered. The monthly and global mean NASA GISS surface temperature index is the red line in (b). The three vertical yellow lines on the right side of (b) highlight the initial condition (1 Jan 2013) and 3–7-yr (2015–19) forecast for a transition to a positive IPO by several different climate models. In (a), the horizontal green lines at 30°N and 30°S mark the approximate location of the seasonal vertically and zonally integrated jet stream. The climatology is 1977–2022 for AAM and 1951–80 for surface temperature. At the top of (a), the plus and minus signs refer to the sign of the anomaly (STJ means subtropical jet).

and the IPO/IPV turns negative. This is discussed further in section 7.

b. *Global NCEP–NCAR Reanalysis-1 (R1 data)*

Global fields from R1 data (Kalnay et al. 1996) were used to determine the seasonal mean changes from P1 to P2 using the standard seasons December–February (DJF), March–May (MAM), June–August (JJA), and September–November (SON). Here we focus on 500-hPa height, although climatology differences for outgoing longwave radiation and 200-hPa streamfunction were also produced. The P2 − P1 seasonal mean 500-hPa height differences are shown in units of geopotential meters.

c. *Sea surface temperature*

The NOAA Extended Reconstructed SST v5 dataset was obtained online (https://downloads.psl.noaa.gov/Datasets/noaa.ersst.v5/sst.mnmean.nc). As with AAM and 500-hPa height, the 1977–2022 climatology is removed to make anomalies. Data are available monthly from January 1958 to December 2022.

3. Two interdecadal states: 1977–98 and 1999–2022

a. *Global and zonal AAM*

Gong et al. (2019) used the R1 data to study long term trends in AAM and its torques during 1948–2016. They found a negative trend in the total torque but a slight positive trend in global AAM signifying an imbalance in the global budget. An earlier study by Paek and Huang (2012) compared five different reanalyses and found very different trends in the datasets. For the longer Twentieth Century Reanalysis (Compo et al. 2006, 2011) there appears to be a positive trend especially in the ERA-20C reanalysis (Veerman and Heerwaarden 2019), but overall, the trends in reanalysis data are not yet consistent. By contrast, Paek and Huang (2012) find that interdecadal variations in global AAM are well reproduced in the reanalysis datasets.

Figure 1 shows global and zonal AAM vertically integrated through all available sigma layers of the assimilating model. The global AAM time series exhibits little trend during 1968–2019 despite the negative trend in the total torques (Gong et al. 2019). Early in the period from 1958 to 1967, the persistent negative values in the tropics and positive values at 20°–30°S result from the surface pressure assimilation error described in the appendix. Strong evidence that these anomalies are spurious comes from the unrealistically low standard deviation of zonal AAM in the tropics and Southern Hemisphere (SH) subtropics before 1968.

AAM displays noticeably different behavior between the two periods P1 and P2 that correspond to different phases of the IPO. P1 has numerous episodes of strong midlatitude/subtropical jet streams with tropical westerly anomalies that often extend poleward into lower midlatitudes at 35°N and 20°S.

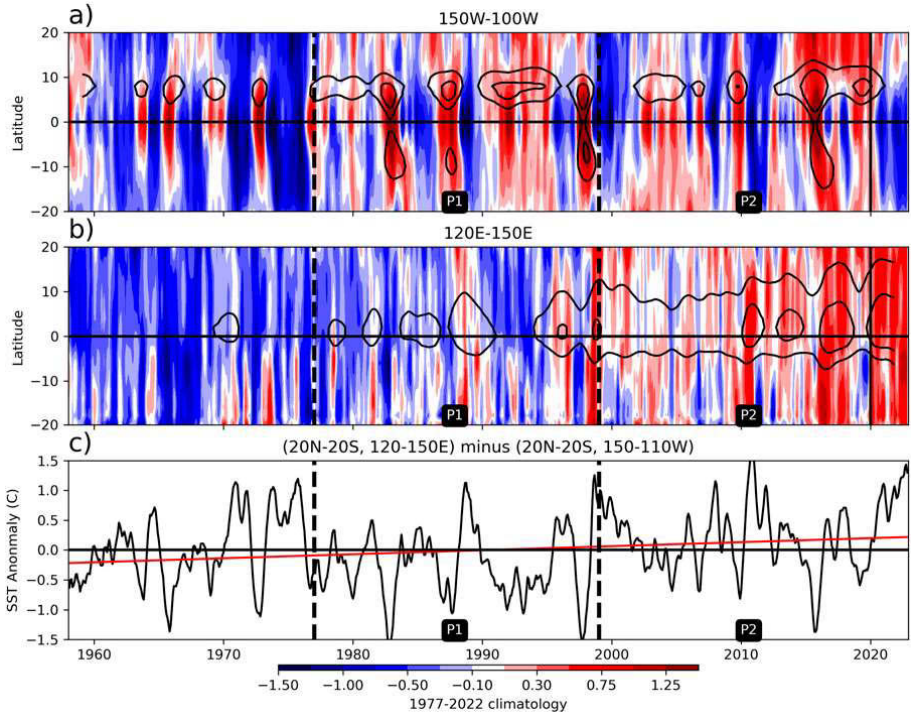

FIG. 2. A longitudinal average of the (a) east Pacific, (b) west Pacific SST anomalies as a function of latitude, and (c) west Pacific minus east Pacific SST (°C) for 1958–2021. The total SST is shown by the black contours: 28° and 28.5°C for (a) and 29° and 29.5°C for (b). El Niño (red shading) and La Niña (blue) episodes are prominent features in the east Pacific sector [(a)], whereas global warming is more evident in the western sector. The red line on (c) is the 1958–2022 trend in SST gradient. The climatology is 1977–2022.

Two episodes of poleward propagation are especially prominent during the 1982/83 and 1997/98 El Niños. Poleward propagation of AAM on interannual time scales has been studied for many years (Dickey et al. 1992; Black et al. 1996) and skillful model predictions of the zonal wind out to about a year may be feasible (Scaife et al. 2022). P2, on the other hand, has mainly episodes of weakened subtropical jets that are anchored by negative–positive–negative zonal mean zonal wind anomalies between 40°N and 40°S that recur nearly every year during P2. Last, a trend toward stronger westerly flow is seen in Fig. 1a along about 60°S that likely is a manifestation of downward coupling from the ozone hole during DJF (Orr et al. 2021). These patterns occur often enough that they project onto the P2 climatology.

Also highlighted in Fig. 1b (yellow lines) are the initial condition and 3–5-yr verification target for climate model predictions of the IPO made by Henley et al. (2017), Meehl et al. (2016b) and Thoma et al. (2015). The 2015–19 period has a weak positive global AAM anomaly, and SSTA have a weaker gradient because of the 2015/16 El Niño. These are consistent with a return to the positive phase of the IPO, and as a result model predictions verified at the 3–5-yr range (Meehl et al. 2022). However, the anomaly pattern of weak subtropical jets continued and recent developments in Pacific Ocean SSTs following the 2015/16 El Niño leave the prediction of IPO positive phase beyond 5 years in doubt.

The red curve in Fig. 1b is the global mean surface temperature anomaly. At first glance it appears to rise steadily through the record, but closer scrutiny reveals accelerated warming during P1 and a hiatus during most of P2. Moreover, each El Niño event produces a jump in temperature and global AAM anomalies as seen in Fig. 1b. After 1997/98, the temperature increase was maintained as part of the warming hiatus (Trenberth et al. 2014; Hu and Fedorov 2017). Likewise, the jump to 1°C after the 2015/16 El Niño appears to be maintained through 2022. Next, we show that SSTs in the western Pacific warm pool track the global temperature curve closely and also warm significantly after the 2015/16 El Niño (see also Kosaka and Xie 2013).

b. *Tropical Pacific sea surface temperature*

Henley et al. (2015) found that the SST gradient across the tropical Pacific Ocean is enhanced during a negative IPO and weakened during the positive phase. The result was obtained using bandpass filtered data so global warming was removed. Figure 2 compares the east (Fig. 2a) and west (Fig. 2b) Pacific Ocean SST anomalies and their west–east difference (Fig. 2c) as a function of latitude. A 3-month running mean is applied to monthly data and the results are only weakly dependent on the longitude or latitude definition of west and east Pacific Ocean.

The shading in Figs. 2a and 2b illustrates a positive temperature trend in each region although the east Pacific trend is

TABLE 1. Southern Hemisphere (SH) and Northern Hemisphere (NH) latitude limits of the 29°C isotherm.

	SH	NH
P1 (1977–98)	1.5°S	4.0°N
P2 (1999–2022)	4.5°S	11.0°N
2016–22	5.5°S	16.5°N

partly masked by ENSO variability. If the data are averaged over 20°N–20°S the west Pacific has a trend of 0.14°C decade^{-1} and the east Pacific has a trend of 0.07°C decade^{-1}. The west warms twice as fast as the east much as expected from the ocean thermostat-type hypothesis (Clement et al. 1996; Sun and Liu 1996). Heede and Fedorov (2023) propose this can reconcile the "slow" ensemble mean CMIP model response to greenhouse gases, and so on, and a fast ocean thermostat response in the observed climate and some climate models.

When the east Pacific is subtracted from the west Pacific as in Fig. 2c, the mean SST difference is −0.25°C during P1 and +0.22°C during P2. Part of the difference is due to the remaining trend in the SST gradient, which is the red line in Fig. 2c. It contributes about 0.2°C of the P2–P1 difference of 0.47. This is a crude measure of internal versus forced variability during 1977–2022.

Figures 2a and 2b also show total SST contours filtered with a 13-month running mean to remove the annual cycle. SSTs greater than 28°C (Fig. 2a) and 29°C (Fig. 2b) are shown. Because the ocean is warming, Leung et al. (2022) found the SST isotherm that supports large (>300 mm) monthly rainfall totals rose from 28.1°C in 1979 to 28.7°C in 2020. Thus, 29°C still provides a good estimate of regions that are likely to experience intense tropical convection. A substantial poleward expansion of the 29°C isotherm is seen in the west Pacific (Fig. 2b) and a slight strengthening of 28°C isotherm in the east Pacific (Fig. 2a). There are large interannual variations of latitude on the order of 7° superimposed on the poleward trend (Fig. 2b), especially during the last 10 years. Many of the poleward surges come with El Niño events.

Table 1 shows the latitude range covered by the 29°C isotherm for P1, P2, and 2016–22. The P1 to P2 poleward movement of 29°C water is 7° latitude or ~3° latitude decade^{-1}. It is more modest in the SH at ~1° latitude decade^{-1}. If the most recent 2016–22 average is used as the endpoint, 29°C now covers 22° of latitude from 5.5°S to 16.5°N versus 5.5° of latitude from 1.5°S to 4.0°N during P1. The Indian Ocean (40°–120°E) shows a similar expansion of 28.5°C water into the NH (not shown).

The current IPWP would favor a continued strong Walker circulation, northern Maritime Continent convection and low AAM, namely, a negative IPO. On the other hand, the Pacific SST gradient is near an all-time high at the end of 2022 and ENSO variability can produce large and rapid changes in SSTs.

4. Period mean anomaly maps

a. Sea surface temperature

Figure 3 shows that the P2 − P1 pattern of SST is positive over most of the globe including the IPWP (~40°–150°E). The main exceptions are the cool anomalies in the SH around 60°S that are linked with strong negative frictional torques (see Hartmann 2022) and those in the east Pacific Ocean that are presumably linked with the IPO's negative phase. Large positive differences in the tropical west Pacific extend toward midlatitudes of the north and South Pacific Ocean (Roxy et al. 2019; Henley et al. 2015; Meehl et al. 2016a). During P1, the 29°C isotherm (not shown) is mostly east of New Guinea, and it is cool in the region of climatological Indonesian convection around 120°–140°E. This eastward expansion of the IPWP in 1976/77 (Miller et al. 1994) was hypothesized to have weakened the Walker circulation and energized the jet stream across the east Pacific and North America.

During P2, the centroid of the warm pool (29°C isotherm) shifted to the northwest and increased in meridional extent, as shown previously in Fig. 2. SST anomalies are now positive

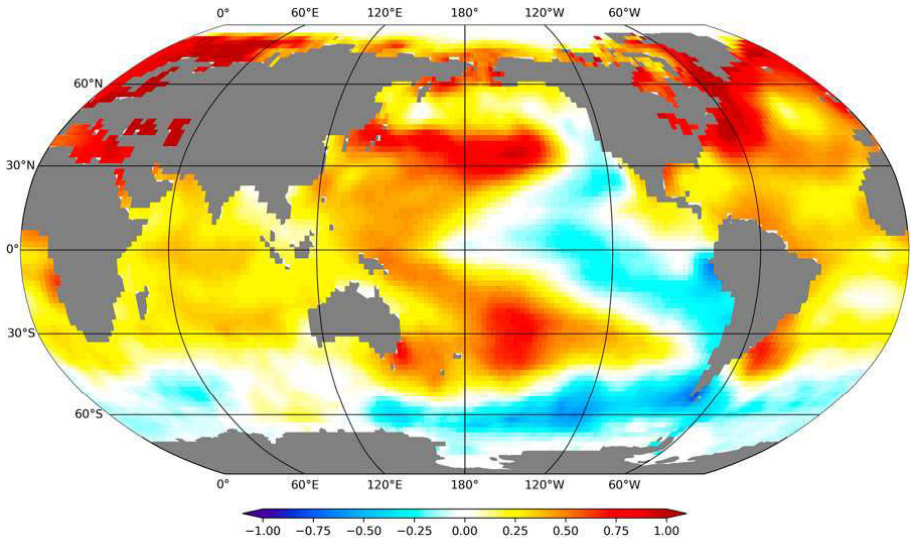

FIG. 3. The P2 − P1 difference in sea surface temperature (°C).

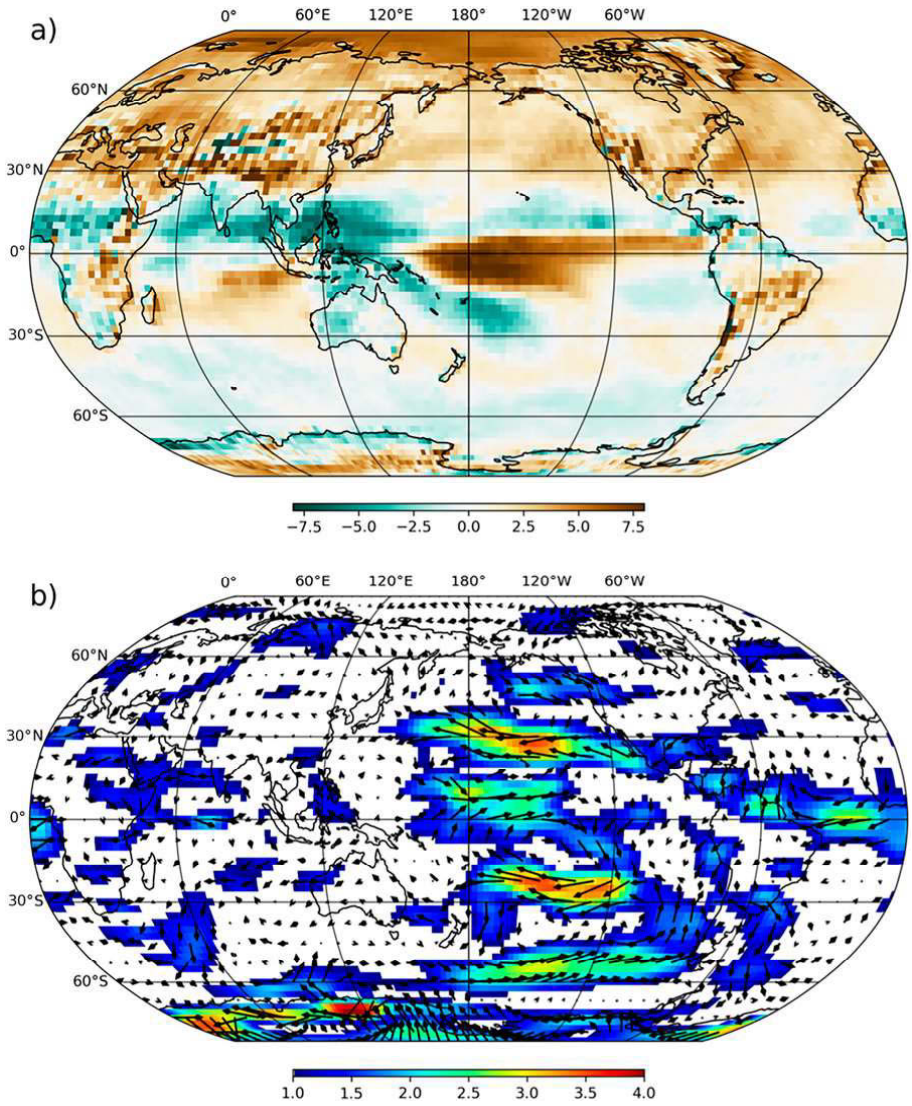

FIG. 4. The P2 − P1 difference in (a) outgoing longwave radiation and (b) 250-hPa vector wind and isotach anomalies. The wind differences have the structure of a wave train emanating from suppressed convection over the tropical central Pacific Ocean as seen in (a) (Trenberth et al. 2014).

in the region of strongest climatological convection around the Maritime Continent.

b. Circulation and outgoing longwave radiation

Figure 4 shows the P2–P1 difference in 250-hPa wind and OLR. The OLR differences show that negative anomalies (enhanced convection) have shifted far to the west and north from P1 to P2 and lie over the northern Indian Ocean along 10°N to past the Philippines consistent with a stronger Walker circulation and the poleward expansion of 29°C water into the NH. During P2, convection occurs west and north of the normal monsoon favoring La Niña and low AAM. Conversely, during P1 negative OLR anomalies are far to the east around the equatorial date line favoring El Niño and high AAM.

Another notable signal is the large positive difference over the northern polar regions. This reflects the positive temperature signal that accompanies Arctic amplification (Cohen et al. 2020; Gong et al. 2020). In the extratropics there are regional signals that reflect well known climate anomalies such as the positive OLR differences over the southwest United States that signal severe drought (Cook et al. 2009). The regional signal across central Asia also suggests drought conditions from eastern Asia west toward the Himalayas in the last ~20 years (Barriopedro et al. 2012). As part of the shift of tropical convection northwestward in P2, tropical Africa along 5°–20°N has seen wet conditions (WMO 2020).

The 250-hPa level is an excellent proxy for the vertical integral of AAM (WS94). Figure 4b shows that the largest differences in the wind field occur from 160° to 90°W and extend nearly pole to pole. The anomalies are only weakly zonally symmetric, and the tropical Pacific differences are consistent with a stronger Walker circulation during P2 and a weaker Walker circulation during P1. The easterly wind differences

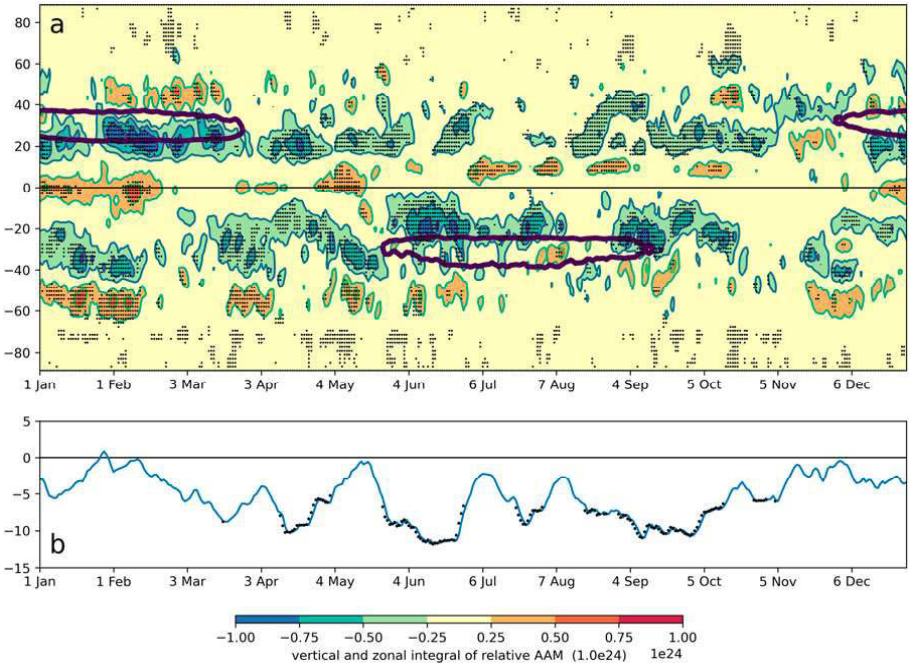

FIG. 5. The P2 climatology minus the P1 climatology for (a) vertical and zonal integrals of relative AAM and (b) global AAM (ordinate units $\times$ 1.0 $\times$ 10^{24}). The heavy lines on (a) mark the location of the climatological "jet stream." The stippling on (a) and (b) denotes local points that pass the 95% two-sided significance test relative to a bootstrapped distribution of differences. Of the 365 $\times$ 94 points, 15.3% are locally significant at the 95% level, which also passes a global significance test at the 95% level (Livezey and Chen 1983).

around 30°N and 25°S imply a southward-shifted jet stream with low pressure extending into North America during P1 and a poleward-shifted jet stream with high pressure extending into western North America during P2. The westerly differences at higher latitudes are stronger in the SH along 55°–60°S.

5. Difference in climatology

a. *Atmospheric angular momentum*

One issue to make explicit is how much the seasonal climate itself has changed between P1 and P2. Normally the climatology is defined using 30-yr periods, but here we compare two ~22-yr periods. The annual cycle of climate change can be determined by averaging a variable of interest across each day of the year for P1 and P2 separately and then taking the difference. All annual harmonics are removed in this process.

Figure 5 illustrates the P2–P1 difference in global and zonal AAM for all latitudes and all days of the year. Negative (positive) values denote anomalous easterlies (westerlies). The contour interval was chosen to be ½ of that used in plots of 5-day averaged AAM (e.g., Fig. 7a). The stippling denotes a 95% statistically significant local anomaly on each panel based on a bootstrapped distribution when sampling from 1968 to 2020. Of 365 $\times$ 94 points, 15.3% are locally significant at the 95% level, which also passes a global significance test at the 95% level (Livezey and Chen 1983).

In Fig. 5 there are two bands of significant negative AAM anomalies over the subtropics of both hemispheres and weaker positive anomalies in the tropics pretty much throughout the year. These are the projection of the nearly yearly easterly–westerly–easterly anomaly episodes seen in Fig. 1a during P2 in comparison with P1. The band of positive (westerly) tropical AAM anomaly develops in boreal fall and moves north with the monsoon during boreal summer. Significant signals are also seen in higher latitudes at 50°N and 50°S, especially during January–March. The heavy contour in Fig. 5a is the location of the seasonal maximum of total AAM, essentially the mean jet stream. The location of anomalies of AAM suggests that westerly flow is weakened south of the jet axis and in some areas enhanced on the north side. This suggests that a weakened and poleward-displaced jet is part of the new climatology, especially in the winter hemisphere.

The global AAM differences (Fig. 5b) display a prominent annual variation with maximum negative anomalies during boreal summer. These align with AAM's seasonal cycle, enhancing the July–August minimum during P2.

b. *500-hPa heights*

A similar analysis documents the period differences in seasonal mean 500-hPa height over the globe. Figure 6 shows the P2 − P1 patterns for the four standard seasons: DJF, MAM, JJA, and SON. All four figures are globally significant at $\gg$95% level, primarily but not exclusively, due to local significance of positive anomalies throughout tropical regions (e.g., Hafez and Almazroui 2014). Overall, positive anomalies (higher heights) are apparent in all seasons

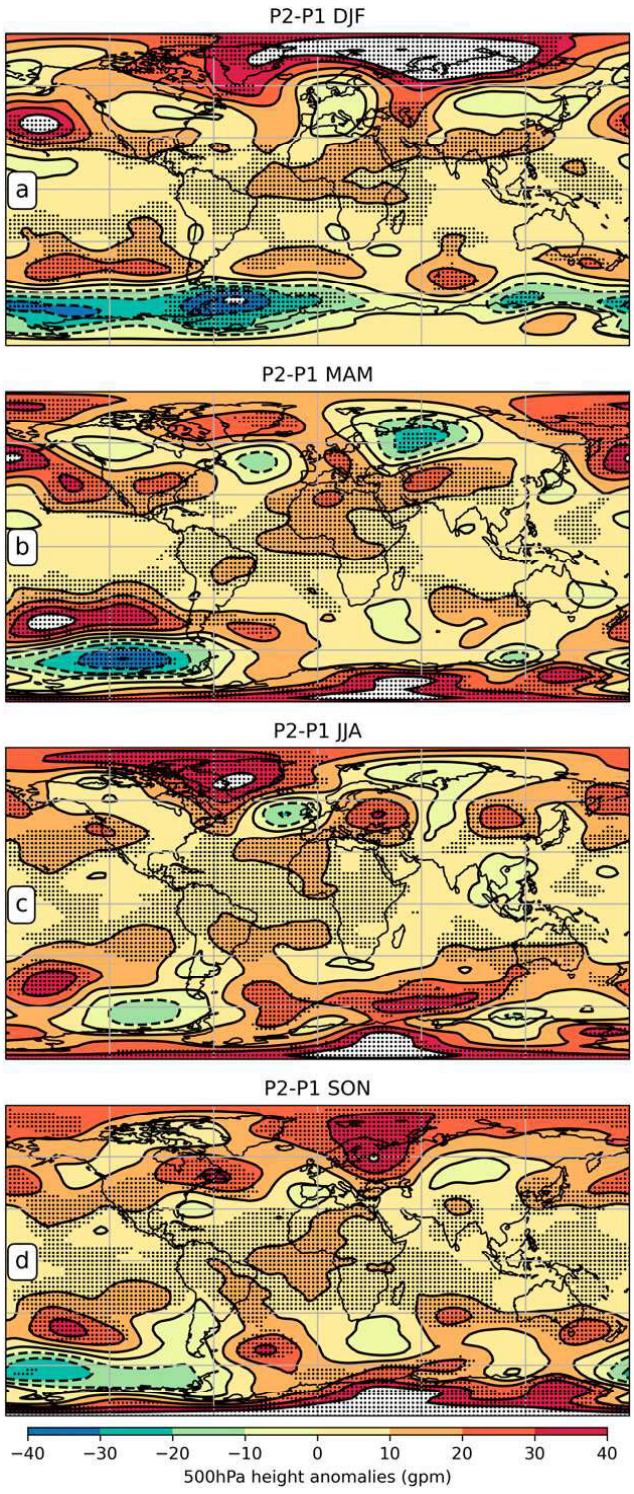

FIG. 6. The P2 climatology minus the P1 climatology for 500-hPa heights for (a) DJF, (b) MAM, (c) JJA, and (d) SON; P2 is 1999–2021, and P1 is 1979–98. The stippling denotes points that are locally significant at the 95% level based on a two-sided bootstrapped distribution of 21-yr mean differences. All four patterns are globally significant at ≫95% level.

consistent with a warming trend over most of the planet from P1 to P2. There are discontinuous zonal bands of positive anomalies in the subtropical to midlatitude regions of both hemispheres. These illustrate regional anomalies that contribute to the zonal and vertical negative AAM anomalies in the 10°–40° latitude bands described in Fig. 5. Ridging over the southwest United States through most of the year signals an ongoing >20-yr drought. Anomalous anticyclones across central Asia suggest drought consistent with precipitation observations (Cook et al. 2009; Williams et al. 2020; Miyan 2014). There is the suggestion of split flows over the eastern Pacific Ocean sometimes extending over North America as the split broadens or shifts.

The meridional height gradient implies strong westerlies along 55°–60°S during DJF and MAM associated with the only significant negative height anomalies over the globe. They have a large zonal average during DJF but are upstream of South America in MAM. Downward dynamical coupling related to the ozone hole is mostly responsible for these westerly zonal wind anomalies and also for a portion of the implied easterly flow anomalies around 20°S that extend to the surface (not shown).

In polar latitudes large positive anomalies extend from Greenland to northeast Siberia during DJF; there is a hint that these may develop over northern Russia during SON and expand over the pole in DJF. The 21-yr mean 500-hPa height anomaly differences exceed 40 GPM over the Arctic in DJF. This is physically consistent with the Arctic warming much faster than the rest of the planet.

6. Recent P2-like variations of the global circulation

In this section two examples of the P2 preferred pattern of weakened subtropical jets are described. One was impacted by a weak El Niño with regular subseasonal activity and the other by a moderate La Niña with sporadic subseasonal activity. Figure 7 shows zonal (Fig. 7a) and global (Fig. 7b) AAM for both total and anomaly fields. MJOs 1–6 during 2019/20 are highlighted on Fig. 7b.

The first sign of the 2020 La Niña in Fig. 7a is the appearance of easterly zonal wind anomalies that persist and lead to persistent negative global AAM anomalies. This occurs ~1 June 2020 when negative zonal wind anomalies start to cover the tropics to subtropics and global AAM anomalies become negative. MJOs 5–6 coincide with global AAM falling from its high boreal winter values and with the global monsoon's seasonal movement toward Asia.

Global AAM shows a regular MJO-related oscillation starting in late 2019 and superimposed on positive time mean anomalies, both of which are consistent with a weak El Niño (see MEI.v2; https://www.psl.noaa.gov/enso/mei/) focused in the central Pacific Ocean. The individual MJOs zonal mean AAM anomalies have distinctive poleward-propagation signals. After MJOs 2–4, the zonal mean westerlies shift into midlatitudes during boreal spring 2020.

The impact of this shift on the total jet stream is shown by highlighting the 6.0×10^{24} kg m^2 s^{-1} contour in Fig. 7a. The movement of positive AAM anomalies poleward acts to extend the NH jet into the boreal spring season with maxima

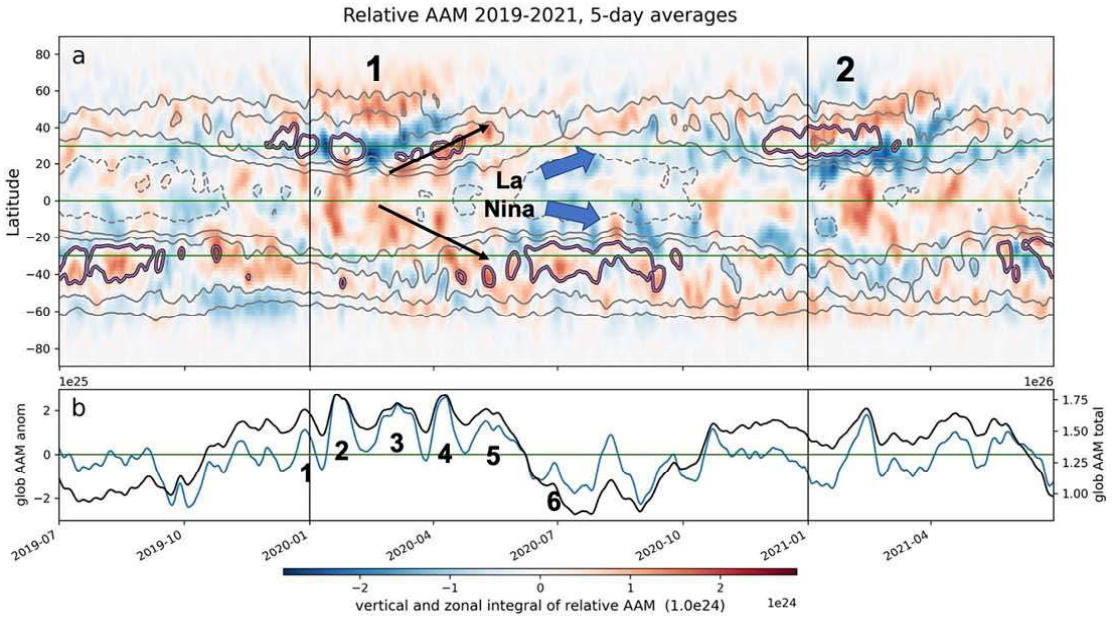

FIG. 7. The (a) zonal and (b) global relative AAM for 1 Jul 2019–30 Jun 2021. Contours in (a) and the black line in (b) denote zonal and global relative AAM. The shading in (a) and blue line in (b) denote relative AAM anomalies. Note the different scale on the left and right ordinates in (b); the black line values are ~5× as large as the blue line values. The two black, solid arrows mark the poleward movement of positive AAM anomalies during 2019/20. A long running La Niña started abruptly in boreal spring 2020 as shown by the blue block arrows, signaling redevelopment of a poleward-shifted jet stream.

near or south of 30°N. The positive anomalies also link to an extensive SH jet along 30°S during astral winter.

The La Niña band of easterly zonal wind anomalies starts ~1 June 2020, initially covers the tropics–subtropics of both hemispheres but then moves to around 30°N and 30°S as the next batch of tropical westerlies associated with MJOs develop during the 2020/21 boreal winter. In contrast with 2019/20, subtropical easterly anomalies persist and strengthen during 2020/21 and the boreal winter jet is weaker and shifted poleward with maxima north of 30°N. The climate is now in a full blown, moderate La Niña and MJO activity is sporadic although a strong event occurs during February 2021.

The La Niña was not unusually difficult to forecast. The Climate Prediction Center (https://www.cpc.ncep.noaa.gov/products/CDB/CDB_Archive_html/CDB_archive.shtml) first called a La Niña watch in June 2020 and went to an advisory in August 2020. Ham et al. (2021) applied deep learning algorithms and showed successful forecasts from June 2020 initial conditions; the skill came from negative Pacific Ocean heat content anomalies moving eastward into the east-central Pacific Ocean. Composites of transitions from El Niño to La Niña over one year by Sharmila et al. (2023) show a similar signal in oceanic heat content.

To diagnose the role of convection and circulation anomalies during April–June 2020 at the onset of the NH summer monsoon, the MJO activity as measured by the Real-Time Multivariate MJO (RMM) index (Wheeler and Hendon 2004) is used. The index describes the MJO but also captures episodes of short-term persistence of OLR and circulation anomalies. Figure 8 depicts three circuits in RMM phase space that line up with MJOs 4, 5, and 6 in the global AAM curve (Fig. 7b). Overall, the 90 days shows phase space trajectories spiraling into the western Indian Ocean and circulation anomalies becoming more La Niña–like.

MJO 4 traverses the circuit coherently and quickly with only a 1–2 day pause over the Indian Ocean around 15 April. The May 2020 MJO starts off over the Maritime Continent but then shifts west back to the Indian Ocean in mid-May and stays for about 10 days accompanied by strongly enhanced low-level convergence over the northern Maritime Continent and trade winds over the west-central Pacific Ocean. When MJO 5 resumes propagating east it makes the circuit quickly and then settles over the Indian Ocean for most of June 2020. The preference for Indian Ocean convection drives AAM lower contributing to the fall seen during MJOs 5 and 6 on Fig. 7b.

We postulate this sequence produced the atmospheric "weather noise" that gives the spring predictability barrier its name. The Niño-3.4 SST index turns negative in May 2020 but then stays small until August–September 2020. Although the possibility of a boost from cool SSTs generated by smoke from the Australian fires (Fasullo et al. 2023) cannot be discounted, the onset of La Niña anomalies appears driven first by the eastward movement of negative Pacific Ocean heat content anomalies around March 2020 and then by anomalous convection anomalies over the Indian Ocean during the May–June 2020 onset of the Asian summer monsoon.

7. Discussion and conclusions

In the presence of external forcing and internal variability, the climate has seen a northwestward shift of large-scale tropical convection, a decrease in global AAM with weaker

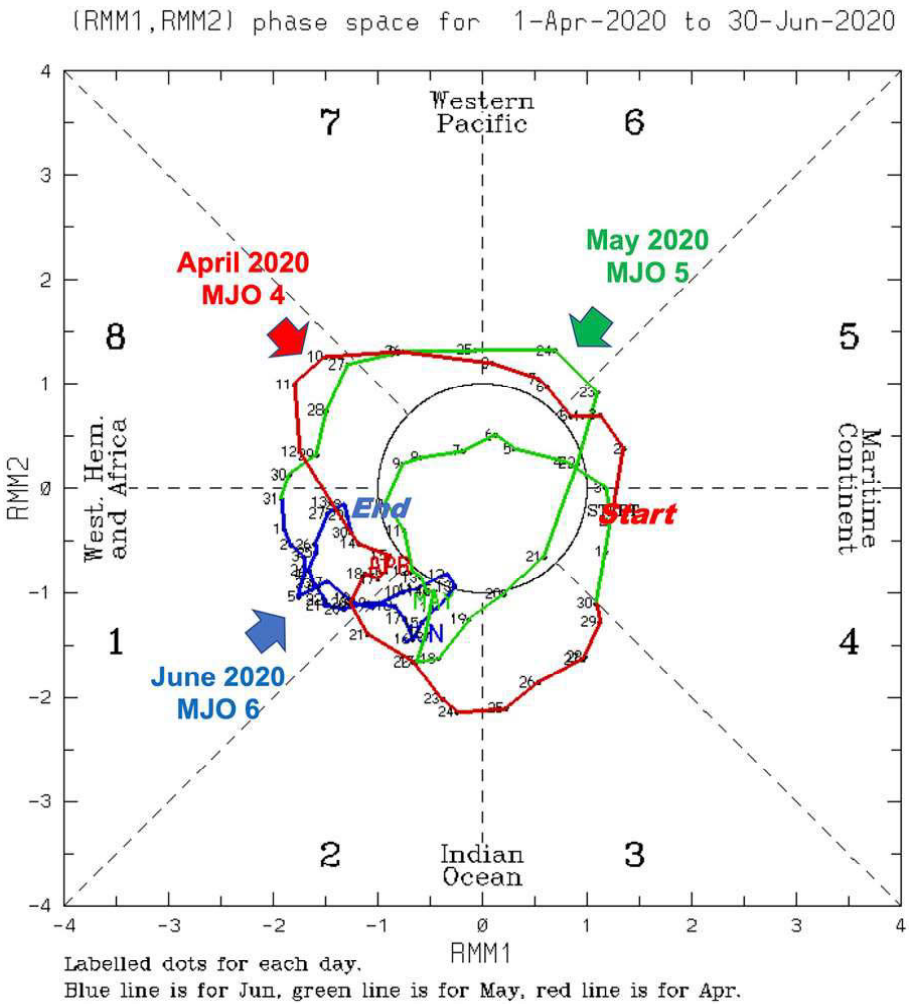

FIG. 8. The Real-Time Multivariate MJO index (Wheeler and Hendon 2004) for April–June 2020. The red line is April 2020, the green line is May 2020, and the blue line is June 2020. The MJO generally makes a counterclockwise circuit in this phase space. The MJO numbers 4–6 are the same as numbers 4–6 on Fig. 7b. Global AAM drops almost 2 sigma during this MJO sequence.

subtropical jets, a poleward expansion of the Indo-Pacific warm pool (IPWP) and a strengthening of the Pacific Ocean SST gradient. Table 2 summarizes specific differences in the global ocean and atmosphere during P1 and P2.

Weller et al. (2016) investigated the role of human caused greenhouse gas emissions on the expansion and increasing heat content of the IPWP and found a dominant component attributable to greenhouse gases and a secondary component attributable to internal PDO variability. In this study, the total P2 − P1 difference in SST anomaly between the west and east Pacific Ocean is 0.47°C while the change contributed by the 1958–2022 trend is 0.2°C. This suggests about equal impact during 1977–2022 from IPO/PDV internal variability and greenhouse gas/aerosol forcing.

In terms of total SST, the 29°C isotherm expanded into the NH at the rate of 2° latitude decade^{-1} with an average location at 17.5°N during the last seven years (2016–22). This is leading to enhanced convective activity from the Indian Ocean to past the Philippines at atypical times of the year. The largest impact may be during the boreal winter; DJF 2023 OLR anomalies (not shown) provide a good example. This regional expansion is much greater than the 0.5° latitude decade^{-1} found by Grise et al. (2019) who used a zonal mean surface wind index to define the width of the tropics.

While climate models successfully predicted a transition to IPO positive during 2015–19, the climate now appears stuck in IPO negative, especially given the increase in SST observed in the west Pacific after the strong 2015/16 and weak 2019/20 El Niños (Fig. 2b). La Niña developed in spring/summer 2020, the start of an amplified, "La Niña–like" P2 pattern that lasted through the 2022/23 boreal winter. As convection shifts seasonally between Southeast Asia and the southwest Pacific Ocean (Meehl 1987), a La Niña–like residual is now more likely given the meridional expansion and shift northwest by the center of the IPWP and its connected circulation anomalies.

As part of the seasonal change in zonal AAM (Fig. 5) and 500-hPa heights (Fig. 6), large and intense subtropical-midlatitude anticyclones have dominated NH continental

TABLE 2. Global climate characteristics of the circulation and ocean surface during period P1 and period P2.

Period P1: 1977–98	Period P2: 1999–2022
High AAM	Low AAM
Indo-Pacific Ocean warm pool expands east; smaller zonal SST gradient	Indo-Pacific Ocean warm pool retreats west; larger zonal SST gradient
Positive phase of the interdecadal Pacific oscillation/Pacific decadal oscillation/Pacific decadal variability	Negative phase of the IPO/PDO/PDV
Equatorial/subtropical anomalous westerly wind flows propagate into the extratropics and support combined midlatitude jet streams, especially from the eastern Pacific Ocean to the Americas	Anomalous easterly wind flows dominate the global subtropics; anomalous equatorial westerlies develop during northern winter and are often "trapped" in the tropics
Strong full-latitude troughs "dig" into western North America and provide plentiful winter–spring rainfall	Strong and persistent subtropical-midlatitude ridges supportive of megadroughts
	Zonal mean positive zonal wind and negative SST anomalies along 60°S

regions during P2 leading to severe droughts especially across southwestern North America (Williams et al. 2020). These ridges have also provided ideal atmospheric conditions for the recent intense wildfire seasons across the western United States as well as other parts of the globe. It is the same ridges, amplified by Rossby wave dispersion linked to subseasonal tropical convective anomalies over the eastern end of the IPWP that have contributed to Arctic amplification since the late 1990s (Gong et al. 2020).

As addressed in considerable detail in IPCC AR6 (IPCC 2021, p. 989), large uncertainty exists of anthropogenic greenhouse gas and aerosol emissions to the future of the planet including whether La Niña– or El Niño–like states will dominate the response. The current overall assessment has "medium confidence that equilibrium warming in response to elevated CO_2 will be characterized by a weakening of the east–west tropical Pacific SST gradient." This does not preclude the possibility of a transient response to greenhouse gases that involves the strengthened SST gradient and expanded IPWP observed during P2 (Heede and Fedorov 2023; Heede et al. 2021).

The other prominent long-term climate feature that shows up in P2–P1 is the negative SST anomaly along 60°S (Fig. 3). It coincides with a negative frictional torque anomaly, especially during DJF, that is linked with deep westerly wind anomalies. These westerlies have been traced to the ozone hole whose zonal mean dynamics was investigated in reanalysis datasets by Orr et al. (2021). Hartmann (2022) even suggests a connection between the ozone hole and the negative SST anomalies in the eastern tropical Pacific Ocean as an alternative to the ocean thermostat hypothesis.

In the SH zonal AAM budget, the negative frictional torque anomaly centered at 60°S is approximately balanced by positive torque anomalies north of 40°S; this includes a positive mountain torque along 10°–30°S that comes primarily from the Andes (Fig. A1a). The torques in the two regions are linked by poleward AAM transports produced by ozone hole dynamics that "saturates" in the early 1990s and the transition to a negative IPO/IPV that occurs abruptly during 1998. Saturates refers to the area of the ozone hole; it climbs rapidly to a maximum from 1979 to 1992, peaks in the early 1990s, and then decreases very slowly thereafter (https://www.eea.europa.eu/en/topics/in-depth/climate-change-mitigation-reducing-emissions/current-state-of-the-ozone-layer). The 60°S friction torque (not shown) also becomes persistent in the early 1990s, that is, when the ozone hole saturates. The positive mountain torque anomalies (Fig. A1a) start to develop in the early 1990s and become persistent in 1998, consistent with a role for both the ozone hole and the transition to P2 or negative IPO.

A positive mountain torque anomaly implies a negative surface pressure anomaly on the west side of the Andes giving enhanced southerly flow west of the mountains and conversely a positive surface pressure anomaly on the east side of the Andes giving enhanced northerly flow east of the mountains. Given the steep terrain from 10° to 30°S, anomalous southerly winds could extend west over the adjacent east Pacific Ocean. In concert with an enhanced Walker circulation and easterly wind anomalies over the tropical Pacific during P2, this provides an additional mechanism for upwelling and advection of negative SST anomalies toward the equatorial east Pacific. It is unclear how well climate models capture the observed mountain torque during 1977–2022 and its related circulation anomalies.

Acknowledgments. This paper is dedicated to the memory of Professor John E. Kutzbach, who taught author Weickmann the importance of paleoclimate for understanding Earth's climate and was a lifelong friend. The authors thank Roland Madden for valuable comments before the paper was submitted. Harry Hendon's comments on the role of the ozone hole in the Southern Hemisphere circulation were also helpful. The project was partially self-funded and partially funded by NSF Grant 2048770 to Professor Victor Gensini, and there are no conflicts of interest for any of the authors.

Data availability statement. The NCEP–NCAR reanalysis data (R1) used during this study are openly available from

NOAA's Physical Sciences Division (https://psl.noaa.gov/data/gridded/data.ncep.reanalysis.html) and are cited in Kalnay et al. (1996). The outgoing longwave radiation (OLR) data are openly available from NOAA's Physical Sciences Division (https://psl.noaa.gov/data/gridded/data.interp_OLR.html) and are cited in Liebmann and Smith (1996). Atmospheric angular momentum (AAM) data were derived from R1 using formulas presented in WS94. The zonal and vertical integrals of AAM are available on request. Sea surface temperature data are the NOAA Extended Reconstructed SST V5. Data information and availability are posted online (https://doi.org/10.7289/V5T72FNM). Global surface temperature data are from GISTEMP Team (2023).

APPENDIX

Spurious Negative Global AAM Anomaly 1958–67

This error note was obtained online (https://psl.noaa.gov/data/reanalysis/problems.shtml):

- "Problem ingesting the surface and mean sea level pressure data affecting the period 1948–67.
- A problem has been uncovered with the encoding of surface and mean sea level pressure that affect the period 1948–67. The problem originated in the erroneous conversion of a portion of the TD13 dataset into the bufr ADPSFC type messages. Details about the effects of the problem are available here."

Unfortunately, the link (http://wwwt.emc.ncep.noaa.gov/gmb/bkistler/psfc/psfc.html) that provides more detail, embedded in "here," is broken.

Here is an example: a 987-hPa surface pressure observation would be erroneously encoded as 1087 hPa. These data would be rejected in the assimilation cycle but then require the 6-h model forecast to come up with the pressure. The model accomplishes this by "predicting" a surface pressure that produces large negative global mountain torques especially along 35°N in the boreal summer. This forces global AAM lower, a state the model apparently prefers when not constrained by observations. We

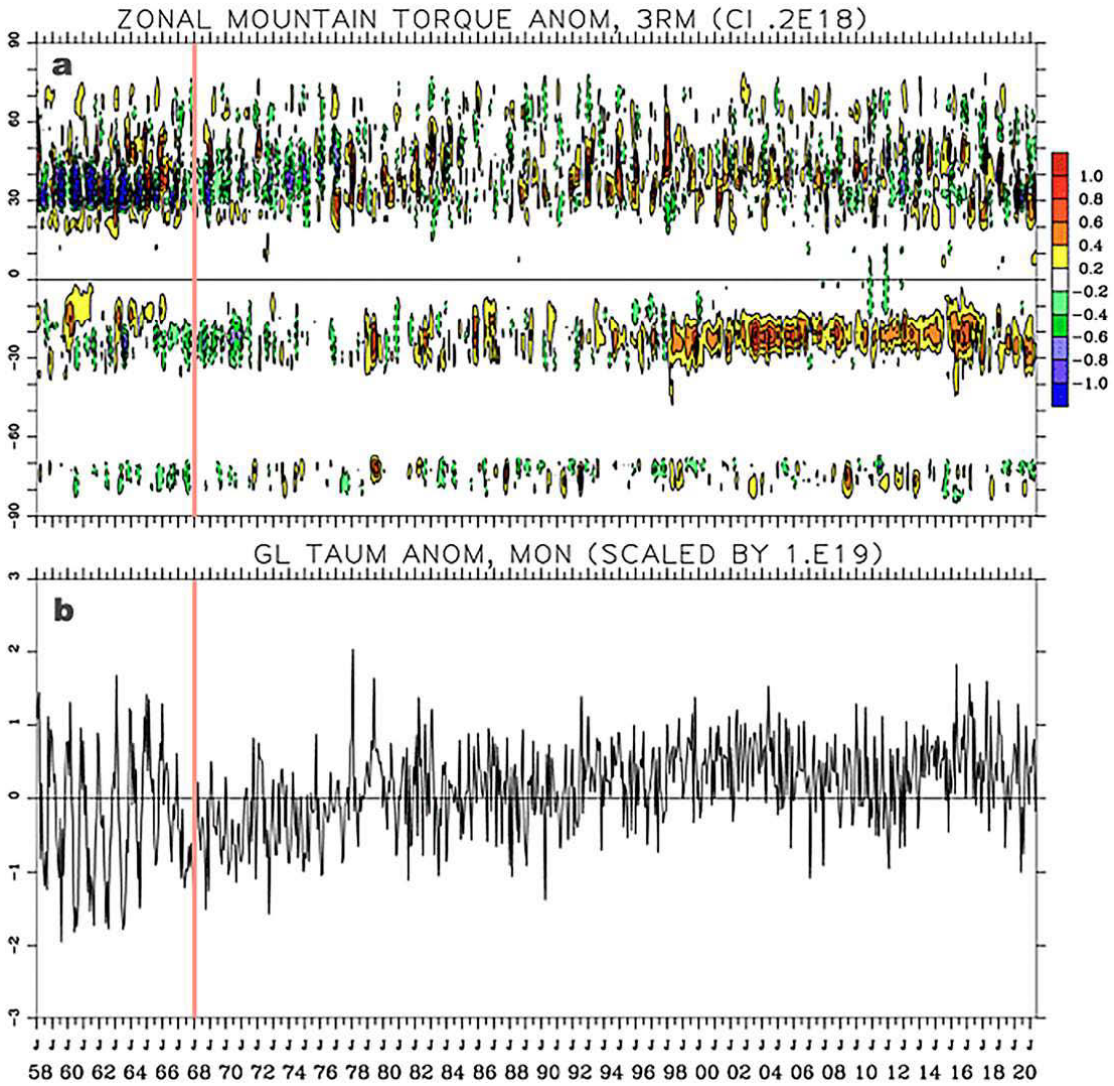

FIG. A1. (a) Zonal and (b) global mountain torque anomalies from the NCEP–NCAR reanalysis, 1958–2021; a 3-month running mean is applied in (a), and monthly data are shown in (b). The red line marks January 1968.

speculate that pressure data during the monsoon over India and around the Tibetan Plateau were especially impacted.

Figure A1 shows the global and zonal mountain torque for the period 1958–2020 from R1. The annual minima in the mountain torque curve seen in Fig. A1b before 1968 occur during boreal summer. From 1958 through 1967 there are large, seasonal oscillations that have negative values in the boreal summer. Their cause can be traced to surface pressure observations that are less than 1000 hPa being left out of the assimilation cycle (Inoue and Matsumoto 2004; Kistler et al. 2001). This introduced a "model preferred" spurious mountain torque that found its way into global AAM. The Himalaya region was particularly influenced by the uncorrected model forecasts. The large unrealistic seasonal cycle has a global mean that is negative, which means the spurious mountain torque forces negative global AAM anomalies. This period was in fact accompanied by unusually persistent upper-level tropical easterlies and SH subtropical westerlies, probably produced by meridional AAM transports linked to the mountain torque. The net effect was to lower global AAM. This problem goes back to 1948 in R1; any trend analysis on AAM using the 1948–67 period should be considered suspect.

REFERENCES

Barriopedro, D., C. M. Gouveia, R. M. Trigo, and L. Wang, 2012: The 2009/10 drought in China: Possible causes and impacts on vegetation. *J. Hydrometeor.*, **13**, 1251–1267, https://doi.org/10.1175/JHM-D-11-074.1.

Black, R. X., D. A. Salstein, and R. D. Rosen, 1996: Interannual modes of variability in atmospheric angular momentum. *J. Climate*, **9**, 2834–2849, https://doi.org/10.1175/1520-0442(1996)009<2834:IMOVIA>2.0.CO;2.

Clement, A. C., R. Seager, M. A. Cane, and S. E. Zebiak, 1996: An ocean dynamical thermostat. *J. Climate*, **9**, 2190–2196, https://doi.org/10.1175/1520-0442(1996)009<2190:AODT>2.0.CO;2.

Cohen, J., and Coauthors, 2020: Divergent consensuses on Arctic amplification influence on midlatitude severe winter weather. *Nat. Climate Change*, **10**, 20–29, https://doi.org/10.1038/s41558-019-0662-y.

Compo, G. P., J. S. Whitaker, and P. D. Sardeshmukh, 2006: Feasibility of a 100-year reanalysis using only surface pressure data. *Bull. Amer. Meteor. Soc.*, **87**, 175–190, https://doi.org/10.1175/BAMS-87-2-175.

——, and Coauthors, 2011: The Twentieth Century Reanalysis project. *Quart. J. Roy. Meteor. Soc.*, **137**, 1–28, https://doi.org/10.1002/qj.776.

Cook, E. R., R. Seager, R. R. Heim Jr., R. S. Vose, C. Herweijer, and C. Woodhouse, 2009: Megadroughts in North America: Placing IPCC projections of hydroclimatic change in a long-term paleoclimate context. *J. Quat. Sci.*, **25**, 48–61, https://doi.org/10.1002/jqs.1303.

Dickey, J. O., S. L. Marcus, and R. Hide, 1992: Global propagation of interannual fluctuations in atmospheric angular momentum. *Nature*, **357**, 484–488, https://doi.org/10.1038/357484a0.

Dong, B., and A. Dai, 2015: The influence of the interdecadal Pacific oscillation on temperature and precipitation over the globe. *Climate Dyn.*, **45**, 2667–2681, https://doi.org/10.1007/s00382-015-2500-x.

Egger, J., K. Weickmann, and K.-P. Hoinka, 2007: Angular momentum in the global atmospheric circulation. *Rev. Geophys.*, **45**, RG400, https://doi.org/10.1029/2006RG000213.

Fasullo, J. T., N. Rosenbloom, and R. Buchholz, 2023: A multiyear tropical Pacific cooling response to recent Australian wildfires in CESM2. *Sci. Adv.*, **9**, eadg1213, https://doi.org/10.1126/sciadv.adg1213.

Folland, C. K., J. A. Renwick, M. J. Salinger, and A. B. Mullan, 2002: Relative influences of the interdecadal Pacific oscillation and ENSO on the South Pacific convergence zone. *Geophys. Res. Let.*, **29**, 1643, https://doi.org/10.1029/2001GL014201.

GISTEMP Team, 2023: GISS Surface Temperature Analysis (GISTEMP), version 4. NASA Goddard Institute for Space Studies, accessed 10 June 2023, https://data.giss.nasa.gov/gistemp/.

Gong, H., M. Huang, L. Zhu, and Y. Shao, 2019: Long-term variations of atmospheric angular momentum and torque. *Meteor. Atmos. Phys.*, **131**, 1697–1711, https://doi.org/10.1007/s00703-019-00663-y.

Gong, T., S. B. Feldstein, and S. Lee, 2020: Rossby wave propagation from the Arctic into the midlatitudes: Does it arise from in situ latent heating or a trans-Arctic wave train? *J. Climate*, **33**, 3619–3633, https://doi.org/10.1175/JCLI-D-18-0780.1.

Grise, K. M., and Coauthors, 2019: Recent tropical expansion: Natural variability or forced response? *J. Climate*, **32**, 1551–1571, https://doi.org/10.1175/JCLI-D-18-0444.1.

Hafez, Y. Y., and M. Almazroui, 2014: Recent study of anomaly of global annual geopotential height and global warming. *Atmos. Climate Sci.*, **4**, 347–357, https://doi.org/10.4236/acs.2014.43035.

Ham, Y.-G., J.-H. Kim, and J.-J. Luo, 2021: Recent progress in ENSO forecast using deep learning. *CLIVAR Exchanges*, No. 81, International CLIVAR Project Office, Southampton, United Kingdom, 3–7, https://doi.org/10.36071/clivar.81.2021.

Hartmann, D., 2022: The Antarctic ozone hole and the pattern effect on climate sensitivity. *Proc. Natl. Acad. Sci. USA*, **119**, e2207889119, https://doi.org/10.1073/pnas.2207889119.

Hartmann, B., and G. Wendler, 2005: The significance of the 1976 Pacific climate shift in the climatology of Alaska. *J. Climate*, **18**, 4824–4839, https://doi.org/10.1175/JCLI3532.1.

Heede, U. K., and A. V. Fedorov, 2023: Colder eastern equatorial Pacific and stronger walker circulation in the early 21st century: Separating the forced response to global warming from natural variability. *Geophys. Res. Lett.*, **50**, e2022GL101020, https://doi.org/10.1029/2022GL101020.

——, ——, and N. J. Burls, 2021: A stronger versus weaker Walker: Understanding model differences in fast and slow tropical Pacific responses to global warming. *Climate Dyn.*, **57**, 2505–2522, https://doi.org/10.1007/s00382-021-05818-5.

Henley, B. J., J. Gergis, D. J. Karoly, S. Power, J. Kennedy, and C. K. Folland, 2015: A tripole index for the interdecadal Pacific oscillation. *Climate Dyn.*, **45**, 3077–3090, https://doi.org/10.1007/s00382-015-2525-1.

——, and Coauthors, 2017: Spatial and temporal agreement in climate model simulations of the interdecadal Pacific oscillation. *Environ. Res. Lett.*, **12**, 044011, https://doi.org/10.1088/1748-9326/aa5cc8.

Hu, S., and A. V. Fedorov, 2017: The extreme El Niño of 2015–2016 and the end of global warming hiatus. *Geophys. Res. Lett.*, **44**, 3816–3824, https://doi.org/10.1002/2017GL072908.

Inoue, T., and J. Matsumoto, 2004: A comparison of summer sea level pressure over east Eurasia between NCEP–NCAR

reanalysis and ERA-40 for the period 1960–99. *J. Meteor. Soc. Japan*, **82**, 951–958.

IPCC, 2021: *Climate Change 2021: The Physical Science Basis.* V. Masson-Delmotte et al., Eds., Cambridge University Press, 2391 pp., https://doi.org/10.1017/9781009157896.

Kalnay, E., and Coauthors, 1996: The NCEP/NCAR 40-Year Reanalysis Project. *Bull. Amer. Meteor. Soc.*, **77**, 437–472, https://doi.org/10.1175/1520-0477(1996)077<0437:TNYRP>2.0.CO;2.

Kistler, R., and Coauthors, 2001: The NCEP–NCAR 50-year reanalysis: Monthly means CD-ROM and documentation. *Bull. Amer. Meteor. Soc.*, **82**, 247–268, https://doi.org/10.1175/1520-0477(2001)082<0247:TNNYRM>2.3.CO;2.

Kosaka, Y., and S. P. Xie, 2013: Recent global-warming hiatus tied to equatorial Pacific surface cooling. *Nature*, **501**, 403–407, https://doi.org/10.1038/nature12534.

Leung, J. C.-H., B. Zhang, Q. Gan, L. Wang, W. Qian, and Z.-Z. Hu, 2022: Differential expansion speeds of Indo-Pacific warm pool and deep convection favoring pool under greenhouse warming. *npj Climate Atmos. Sci.*, **5**, 97, https://doi.org/10.1038/s41612-022-00315-w.

Liebmann, B., and C. A. Smith, 1996: Description of a complete (interpolated) OLR dataset. *Bull. Amer. Meteor. Soc.*, **77**, 1275–1277, https://doi.org/10.1175/1520-0477-77.6.1274.

Livezey, R. E., and W. Y. Chen, 1983: Statistical field significance and its determination by Monte Carlo techniques. *Mon. Wea. Rev.*, **111**, 46–59, https://doi.org/10.1175/1520-0493(1983)111<0046:SFSAID>2.0.CO;2.

Madden, R. A., and P. R. Julian, 1971: Detection of a 40–50 day oscillation in the zonal wind. *J. Atmos. Sci.*, **28**, 702–708, https://doi.org/10.1175/1520-0469(1971)028<0702:DOADOI>2.0.CO;2.

——, and ——, 1972: Description of global-scale circulation cells in the tropics with a 40–50 day period. *J. Atmos. Sci.*, **29**, 1109–1123, https://doi.org/10.1175/1520-0469(1972)029<1109:DOGSCC>2.0.CO;2.

——, and ——, 1994: Observations of the 40–50-day tropical oscillation—A review. *Mon. Wea. Rev.*, **122**, 814–837, https://doi.org/10.1175/1520-0493(1994)122<0814:OOTDTO>2.0.CO;2.

Medhaug, I., M. B. Stolpe, E. M. Fischer, and R. Knutti, 2017: Reconciling controversies about the 'global warming hiatus.' *Nature*, **545**, 41–47, https://doi.org/10.1038/nature22315.

Meehl, G. A., 1987: The annual cycle and interannual variability in the tropical Pacific and Indian Ocean regions. *Mon. Wea. Rev.*, **115**, 27–50, https://doi.org/10.1175/1520-0493(1987)115<0027:TACAIV>2.0.CO;2.

——, A. Hu, B. D. Santer, and S.-P. Xie, 2016a: Contribution of the interdecadal Pacific oscillation to twentieth-century global surface temperature trends. *Nat. Climate Change*, **6**, 1005–1008, https://doi.org/10.1038/nclimate3107.

——, Hu, A., and H. Teng, 2016b: Initialized decadal prediction for transition to positive phase of the interdecadal Pacific oscillation. *Nat. Commun.*, **7**, 11718, https://doi.org/10.1038/ncomms11718.

——, H. Teng, A. Capotondi, and A. Hu, 2021: The role of interannual ENSO events in decadal timescale transitions of the interdecadal Pacific oscillation. *Climate Dyn.*, **57**, 1933–1951, https://doi.org/10.1007/s00382-021-05784-y.

——, ——, D. Smith, S. Yeager, W. Merryfield, F. Doblas-Reyes, and A. Glanville, 2022: The effects of bias, drift, and trends in calculating anomalies for evaluating skill of seasonal-to-decadal initialized climate predictions. *Climate Dyn.*, **59**, 3373–3389, https://doi.org/10.1007/s00382-022-06272-7.

Miller, A. J., D. R. Cayan, T. P. Brnett, N. E. Graham, and J. M. Oberhuber, 1994: The 1976–77 climate shift of the Pacific Ocean. *Oceanography*, **7**, 21–26, https://doi.org/10.5670/oceanog.1994.11.

Miyan, M. A., 2014: Droughts in Asian least developed countries: Vulnerability and sustainability. *Wea. Climate Extremes*, **7**, 8–23, https://doi.org/10.1016/j.wace.2014.06.003.

Moron, V., R. Vautard, and M. Ghil, 1998: Trends, interdecadal and interannual oscillations in global sea-surface temperatures. *Climate Dyn.*, **14**, 545–569, https://doi.org/10.1007/s003820050241.

Nigam, S., A. Sengupta, and A. Ruiz-Barradas, 2020: Atlantic–Pacific links in observed multidecadal SST variability: Is the Atlantic multidecadal oscillation's phase reversal orchestrated by the Pacific decadal oscillation? *J. Climate*, **33**, 5479–5505, https://doi.org/10.1175/JCLI-D-19-0880.1.

Orr, A., H. Lu, P. Martineau, E. P. Gerber, G. J. Marshall, and T. J. Bracegirdle, 2021: Is our dynamical understanding of the circulation changes associated with the Antarctic ozone hole sensitive to the choice of reanalysis dataset? *Atmos. Chem. Phys.*, **21**, 7451–7472, https://doi.org/10.5194/acp-21-7451-2021.

Paek, H., and H.-P. Huang, 2012: A comparison of decadal-to-interdecadal variability and trend in reanalysis datasets using atmospheric angular momentum. *J. Climate*, **25**, 4750–4758, https://doi.org/10.1175/JCLI-D-11-00358.1.

Palmen, E., and C. W. Newton, 1969: *Atmospheric Circulation Systems: Their Structural and Physical Interpretation*. Academic Press, 626 pp.

Peixoto, J. P., and A. H. Oort, 1992: *Physics of Climate*. 1st ed. American Institute of Physics, 520 pp.

Rosen, R. D., and D. A. Salstein, 1983: Variations in atmospheric angular momentum on global and regional scales and the length of day. *J. Geophys. Res.*, **88**, 5451–5470, https://doi.org/10.1029/JC088iC09p05451.

——, ——, T. M. Eubanks, J. O. Dickey, and J. A. Stepp, 1984: An El Nino signal in atmospheric angular momentum and Earth rotation. *Science*, **225**, 411–414, https://doi.org/10.1126/science.225.4660.411.

Roxy, M. K., P. Dasgupta, M. J. McPhaden, T. Suematsu, C. Zhang, and D. Kim, 2019: Twofold expansion of the Indo-Pacific warm pool warps the MJO life cycle. *Nature*, **575**, 647–651, https://doi.org/10.1038/s41586-019-1764-4.

Salstein, D. A., D. M. Khan, A. J. Miller, and R. D. Rosen, 1993: The Sub-bureau for Atmospheric Angular Momentum of the International Earth Rotation Service: A meteorological data center with geodetic applications. *Bull. Amer. Meteor. Soc.*, **74**, 67–80, https://doi.org/10.1175/1520-0477(1993)074<0067:TSBFAA>2.0.CO;2.

Scaife, A. A., and Coauthors, 2022: Long-range predictability of extratropical climate and the length of day. *Nat. Geosci.*, **15**, 789–793, https://doi.org/10.1038/s41561-022-01037-7.

Sharmila, S., H. Hendon, O. Alves, A. Weisheimer, and M. Balmaseda, 2023: Contrasting El Niño–La Niña predictability and prediction skill in 2-year reforecasts of the twentieth century. *J. Climate*, **36**, 1269–1285, https://doi.org/10.1175/JCLI-D-22-0028.1.

Starr, V. P., 1948: An essay on the general circulation of the Earth's atmosphere. *J. Meteor.*, **5**, 39–43, https://doi.org/10.1175/1520-0469(1948)005<0039:AEOTGC>2.0.CO;2.

——, 1951: A note on the eddy transport of angular momentum. *Quart. J. Roy. Meteor. Soc.*, **77**, 44–50, https://doi.org/10.1002/qj.49707733105.

Su, J., R. Zhang, and H. Wang, 2017: Consecutive record-breaking high temperatures marked the handover from hiatus to

accelerated warming. *Sci. Rep.*, **7**, 43735, https://doi.org/10.1038/srep43735.

Sun, D.-Z., and Z. Liu, 1996: Dynamic ocean-atmosphere coupling: A thermostat for the tropics. *Science*, **272**, 1148–1150, https://doi.org/10.1126/science.272.5265.1148.

Thoma, M., R. J. Greatbatch, C. Kadow, and R. Gerdes, 2015: Decadal hindcasts initialized using observed surface wind stress: Evaluation and prediction out to 2024. *Geophys. Res. Lett.*, **42**, 6454–6461, https://doi.org/10.1002/2015GL064833.

Trenberth, K., J. T. Fasullo, G. Branstator, and A. S. Phillips, 2014: Seasonal aspects of the recent pause in surface warming. *Nat. Climate Change*, **4**, 911–916, https://doi.org/10.1038/nclimate2341.

Tung, K.-K., X. Chen, J. Zhou, and K.-F. Li, 2019: Interdecadal variability in pan-Pacific and global SST, revisited. *Climate Dyn.*, **52**, 2145–2157, https://doi.org/10.1007/s00382-018-4240-1.

Veerman, M. A., and C. C. van Heerwaarden, 2019: Trends in and closure of the atmospheric angular momentum budget in the 20th century in ERA-20C. *Quart. J. Roy. Meteor. Soc.*, **145**, 2990–3003, https://doi.org/10.1002/qj.3600.

Weickmann, K., 2003: Mountains, the global frictional torque, and the circulation over the Pacific–North American region. *Mon. Wea. Rev.*, **131**, 2608–2622, https://doi.org/10.1175/1520-0493(2003)131<2608:MTGFTA>2.0.CO;2.

Weickmann, K. M., and P. D. Sardeshmukh, 1994: The atmospheric angular momentum cycle associated with a Madden–Julian oscillation. *J. Atmos. Sci.*, **51**, 3194–3208, https://doi.org/10.1175/1520-0469(1994)051<3194:TAAMCA>2.0.CO;2.

——, G. N. Kiladis, and P. D. Sardeshmukh, 1997: The dynamics of intraseasonal atmospheric angular momentum oscillations. *J. Atmos. Sci.*, **54**, 1445–1461, https://doi.org/10.1175/1520-0469(1997)054<1445:TDOIAA>2.0.CO;2.

Weller, E., S.-K. Min, W. Cai, F. W. Zwiers, Y.-H. Kim, and D. Lee, 2016: Human-caused Indo-Pacific warm pool expansion. *Sci. Adv.*, **2**, e1501719, https://doi.org/10.1126/sciadv.1501719.

Wheeler, M. C., and H. H. Hendon, 2004: An all-season real-time multivariate MJO index: Development of an index for monitoring and prediction. *Mon. Wea. Rev.*, **132**, 1917–1932, https://doi.org/10.1175/1520-0493(2004)132<1917:AARMMI>2.0.CO;2.

Williams, A. P., and Coauthors, 2020: Large contribution from anthropogenic warming to an emerging North American megadrought. *Science*, **368**, 314–318, https://doi.org/10.1126/science.aaz9600; Corrigendum, **370**, eabf3676, https://doi.org/10.1126/science.abf3676.

World Meteorological Organization, 2020: State of the Global Climate 2020. WMO Provisional Rep., 38 pp.

Yang, D., J. M. Arblaster, G. A. Meehl, M. H. England, E.-P. Lim, S. Bates, and N. Rosenbloom, 2020: Role of tropical variability in driving decadal shifts in the Southern Hemisphere summertime eddy-driven jet. *J. Climate*, **33**, 5445–5463, https://doi.org/10.1175/JCLI-D-19-0604.1.